

Experimental Investigation and Modeling of the Ignition Transient of a Coaxial H₂/O₂-Injector

V. Schmidt, D. Klimenko, O. Haidn, M. Oschwald
DLR Lampoldshausen, Institute of Space Propulsion
D-74239 Hardthausen, Germany

A. Nicole, G. Ordonneau, M. Habiballah
ONERA Chatillon, Fundamental and Applied Energetics Department
BP 72, 92322 Chatillon, France

October 14, 2003

Abstract

A test case have been defined to investigate experimentally and by numerical simulation the transient ignition phenomenology when igniting coaxial injected O₂ and H₂ by a laser. Using high-speed photography the temporal evolution of the flame and its anchoring at the injector could be visualized. From the analysis of the flame front movement flame velocities and convection velocities have been determined at specific phases during the ignition transient. Numerical simulation of ignition transient were undertaken in two different situations : the microcombustor which was investigated experimentally and which objective is to get insight with basic processes involved in H₂/O₂ ignition and the VINCI engine as a support to the development program.

For the micro combustor, as a first step, 2D axisymmetrical calculations were performed and allowed to adjust computational geometry, laser ignition modeling and a series of parametric studies. Preliminary ignitions results are presented. 3D simulations were also undertaken, but large computational time induced by the complex physical structure and the 3D geometry could not enable to finalize them. Nevertheless, some preliminary results are presented here.

Finally, using some simplifying hypotheses, numerical simulation of the Vinci engine transient ignition is presented.

1 Introduction

The ignition of the propellants injected into a rocket combustion chamber and the subsequent propagation and anchoring of the flame is an important design consideration for all types of rockets [1]. Reliable ignition has to be guaranteed and the initiated turbulent diffusion flame has to stabilize without overpressure or blow out. The analysis of this process has to take into account that the boundary conditions for the flame are changing until stationary combustion chamber conditions are reached: during the ignition transient the pressure is increasing, due to the thermal transient in the injector head the velocities of the injected fluids are changing or the propellants may even change their phase. Atomization is adjusting to the transient injection conditions and the flow field in the combustion chamber has to adapt continuously to the actual status of the flame as well.

The motivation to address the problem of ignition is based on several aspects. The ability to launch multiple payloads into orbit in one flight is an essential feature of the Ariane launcher family with relevant impact on costs/payload. A new cryogenic upper stage with a new cryogenic engine named VINCI is currently under development aiming to increase the payload capacity of

Ariane 5 to 12 tons [2]. Engine architecture is based on an expander cycle in order to match requirements for low cost and reliable multiple ignitions under vacuum conditions. This has initiated igniter development and ignition research activities [3], [4], [5]. Experiences in former development programs have shown how important a sound understanding of the ignition process is. Anomalies during the ignition process of the HM7 engine resulted in the loss of the Ariane flights V15 and V18 [6]. Another motivation to get more insight into the ignition transient of a coaxial injected cryogenic H_2/O_2 is based on the observation that low- and high-frequency combustion instabilities may develop during this transient [7].

Predictivity of the models and numerical tools to analyze the ignition transient has still limitations. In H_2/O_2 -rocket combustors the injected propellants are ignited by a stream of hot gas originating the igniter device. The hot gases have to mix with the injected propellants and to initiate combustion in a situation which is characterized by strong spatial inhomogeneities e.g. in respect to species, temperature, turbulence and state of mixing. Turbulent transport properties are mainly controlling mixing. The problem of rocket combustor ignition has motivated several experimental investigations [8], [9], [10], [11], [12], [13] and was addressed by modeling and numerical simulation [4], [14], [15]. However, the problem of reliable prediction of the ignition transient in a compressible, reactive, instationary flow is still pending. Where are regions with ignitable mixtures in the flow? Is the mixing of the igniter jet with the injected propellants efficient? Is there sufficient energy transfer of the hot igniter gases to these regions? When combustion has been initiated, what are then the dominant parameters controlling the flame propagation and stabilization? How can flame blow out and high overpressure during the ignition transient be prevented?

This paper presents both experimental and numerical simulations of oxygen/hydrogen ignition transient. The objective is to get an insight into main processes involved in the ignition of cryogenic engines like the VINCI.

The paper comprises two parts : the first one is devoted to fundamental research studies on ignition physics using the DLR GOx/GH2 single element combustor, ignited by a laser source. Experimental and preliminary results are presented. The second part deals with numerical simulation of the VINCI engine ignition as a support of the development project. This second activity performed in parallel to fundamental activities makes use of current models and simplified configuration.

2 Experimental Investigation of O_2/H_2 -ignition transient

2.1 Experimental set-up

2.1.1 Combustion Chamber

The tests have been done at the M3 test-facility at DLR Lampoldshausen. The micro-combustor has a square cross section ($6 \times 6\text{cm}^2$) and a length of 14cm (Figure 1). It is designed for combustion chamber pressures up to 2MPa. Operation time of the capacitively cooled combustor under hot fire conditions is limited to 1-2s. Quartz windows give complete optical access to the combustor volume. Two slid windows in the upper and lower combustor wall allow access for the igniting laser. The chamber nozzle has a diameter of 6 mm. Optional a nozzle with 4mm diameter could be mounted.

The gaseous propellants at ambient temperature have been injected through a single coaxial injector. The diameter of the O_2 -post (1.22mm) is fixed. The outer O_2 -post diameter, i.e. the inner diameter of the H_2 annular slit, is 2.0mm. The cross section of the annular H_2 -slit can be varied by exchanging the ring defining the outer H_2 -slit diameter and was 4.0mm in the tests presented in this paper.

The chamber is continuously purged with nitrogen prior to a test, the N_2 -purge is shut off 1s before the H_2 -valve is opened. The O_2 -valve is opened 20ms after the H_2 -valve.

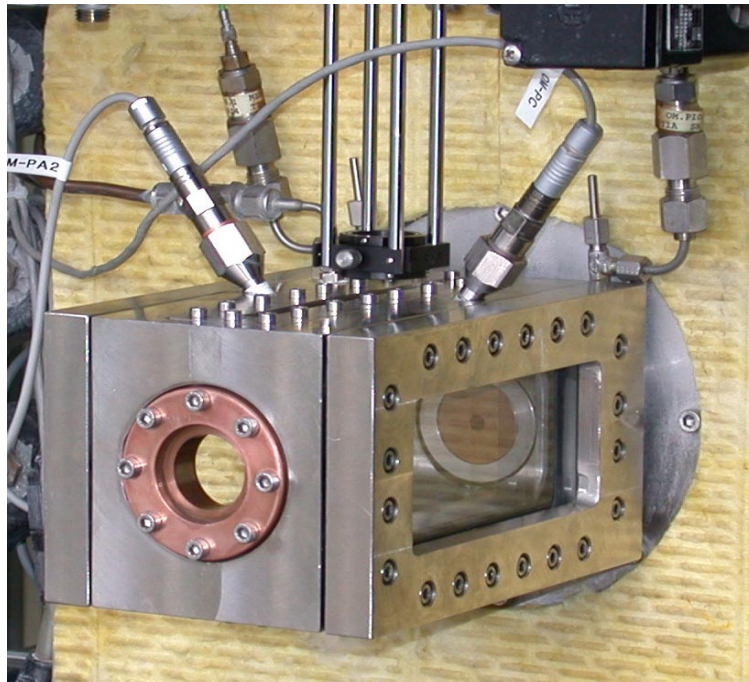


Figure 1 : Photograph of the micro-combustor

2.1.2 Laser Ignition

Combustion is initiated in these tests by laser induced gas break down. A frequency doubled Nd:YAG laser (523nm, 195mJ/pulse) is focused into the flow. The focus position was $z=36\text{mm}$ downstream the injector exit and $r=2.5\text{mm}$ off-axis from the O_2 -jet.

Laser ignition allows full control of the time of ignition, which is essential for synchronization of the data acquisition systems with the ignition transient. Furthermore as compared to electric spark ignition which has been used by several authors [9], [10], [11], [12], laser ignition gives high flexibility in choosing the location of energy release. The location of ignition can be chosen to be in the central flow region without disturbing this flow by the ignition equipment.

Laser induced gas-break down has been studied intensively since it has been first reported in 1963 by Maker et al. [16]. The leading part of the laser pulse is transmitted in the focal volume until the ionization threshold intensity has been reached. As soon as a plasma is formed laser radiation from later parts in the pulse is absorbed efficiently [17]. Since in our set-up a measurement of the transmitted radiation was not possible, the energy deposited in the flow cannot be deduced. However, our pulse energy is far above the energy required for ignition of H_2/O_2 -mixtures near the flammability limit at ambient conditions [18], thus the major part of the pulse energy is assumed to be absorbed.

The expansion of the plasma immediately after laser absorption results in the formation of an shock front that becomes spherical in time. This blast wave expands and an estimation of McManus et al. for electric spark ignition has shown that the shock heating of the mixture is not probable [8]. During laser absorption the temperature in the plasma can reach several 10^4K [19]. In the following the plasma cools down by adiabatic expansion. From Schlieren images at about $30\mu\text{s}$ after the laser pulse we determined that the bubble of hot gas had an ellipsoidal shape with an extension of 2mm in axial and of 3.5mm in radial direction. The extension in the radial direction is in the order of the distance of the laser focus from the central axis of the O_2 -jet. The

flow induced by the expanding hot gas is therefore probably changing the local parameters in the shear layer between O₂-jet and hydrogen co-flow.

Tests have been performed with different pulse energies of the ignition laser. No influence of the pulse energy on the temporal evolution of the OH-emission or combustion chamber pressure has been found. It can therefore be assumed the results are not biased by ignition energies in the range from 80mJ to 195mJ.

2.1.3 Diagnostic Techniques

Schlieren Photography: A color-Schlieren set-up has been used to visualize the flow topology. Images have been recorded with a Hasselblad film camera.

Rayleigh Scattering: Using the radiation of an KrF-excimer laser (248nm) a planar light sheet has been illuminated in the flow. An intensified CCD-camera detected the Rayleigh signal. The Rayleigh scattering cross section of O₂ is 3.9 times that of H₂, allowing the observation of the disintegration of the oxygen jet in the annular flow of hydrogen. Under favorable conditions even quantitative mixture ratios can be obtained.

OH-Imaging: The flame evolution is recorded with an intensified high-speed CCD-camera with a interference filter that only transmits light in the range of 300-310nm, i.e. radiation emitted by the OH-radical. The Photron Fastcam Ultima I² allows recording images at a frame rate of 18KHz at a resolution of 256x128 pixel, the dynamic range was 8bit. In regions without chemical activity less than 2 counts have been recorded on the detector. Therefore all pixels with 3 counts or more have been assumed to belong to the flame.

In each frame of the OH-image series the coordinates of flame-pixels at the most upstream position z_U and downstream position z_D have been determined. From these data the velocities at the upstream and downstream flame front as seen by an observer in the laboratory coordinate system can be calculated according to

$$v_U = \frac{z_U(t_{i+1}) - z_U(t_i)}{\Delta t}$$

where Δt is the time between two frames. Similarly the downstream front velocity v_D is determined. The upstream front moves with the difference of flame velocity v_F and convection velocity v_C

$$v_U(z_U) = v_C(z_U) - v_F(z_U)$$

and the downstream front moves with

$$v_D(z_D) = v_C(z_D) + v_F(z_D)$$

With the assumption that the flame- and convection-velocities at $z = z_D$ and $z = z_F$ are identical the flame velocity

$$v_F = \frac{v_D - v_U}{2}$$

as seen by an observer moving with the flow with the convection velocity

$$v_C = \frac{v_D + v_U}{2}$$

can be estimated:

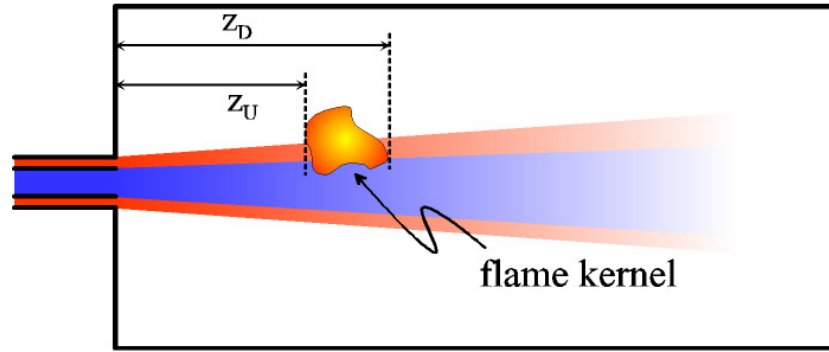


Figure 2 : Determination of the upstream and downstream flame position

2.2 Test Conditions

The tests presented here have been done at ambient temperature and ambient pressure in the combustion chamber prior to ignition. The propellants have been injected in the gaseous state and ignition has been initiated after stationary cold flow conditions have been approached. Tests have been done at a mixture ratio of $R_{OF}=2$.

The injection conditions as calculated for injector exit are given in table 1. The mass flows are determined experimentally. The values of the momentum flux and velocity ratios are calculated based on estimated injection velocities. The injection conditions as calculated for the injector exit are given in Table 1. The mass flows are determined experimentally. The values of the momentum flux and velocity ratios are calculated based on estimated injection velocities. The injection conditions match realistic conditions in terms of Reynolds-numbers for hydrogen and oxygen. Taking data from Baudart et al. [15] momentum flux ratios $J=(\rho v^2)_{H_2}/(\rho v^2)_{O_2}$ ranging from 0.002 to 0.3 can be estimated at ignition conditions in cryogenic rocket combustors. The integral H_2 -momentum flux $I_{H_2}=(\rho v^2 A)_{H_2}$ which has appeared to be an important parameter to characterize the ignition transient phenomena in the former experiments [13] is given as well in Table 1.

m_{H_2} [g/s]	m_{O_2} [g/s]	Re_{H_2}	Re_{O_2}	J	v-ratio	I_{H_2} [kg·m/s ²]
0.58	1.15	18616	43836	~0.2	~1.8	~0.4

Table 1 : Injection conditions.

2.3 Results

2.3.1 Conditions before Ignition

A Schlieren image taken 35 μ s after ignition is shown in Figure 3. The laser induced flame kernel has just developed and the wake of hot gas can be seen. The O_2 -jet upstream this kernel is still not influenced by the flame and the regular pattern of Mach knots is clearly visible in the sonic O_2 -jet leaving the injector.

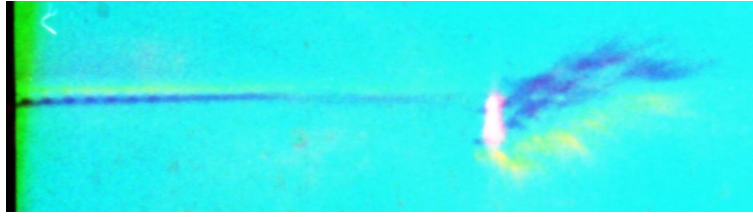


Figure 3: Schlieren image 35 μ s after ignition

Single pulse images of the Rayleigh scattering signal are shown in Figure 4. The O₂-jet visible due to its high Rayleigh scattering cross section as compared to H₂ shows an increasing zigzag-like shape on its way downstream until it disintegrates into separate regions of high O₂-density. The zigzag bending - although not strictly regular - seem to match the periodicity of regular Mach disk pattern of the sonic O₂-jet seen in the Schlieren images.

Rayleigh images from several single shots were averaged to increase signal-to-noise ratio and the data have been normalized for the intensity distribution in the laser light-sheet. Radial profiles of the Rayleigh signal have been extracted from these images averaged over 2mm in axial direction. The results are shown in figure 5 for $z=12-14$ mm, $z=22-24$ mm and $z=32-34$ mm. The high Rayleigh intensity on the central line clearly reflects the high O₂-density, which is decreasing downstream. The width of the O₂-jet is broadening with increasing distance to the injector. At large radii the Rayleigh signal is increasing with z , indicating increasing enrichment of O₂ in the background gas downstream. For $z=12-14$ mm an increase of Rayleigh signal is observed for $r>5$ mm which cannot be explained up to now. A possible reason may be condensation of water vapor from previous experiments on the quartz-windows.

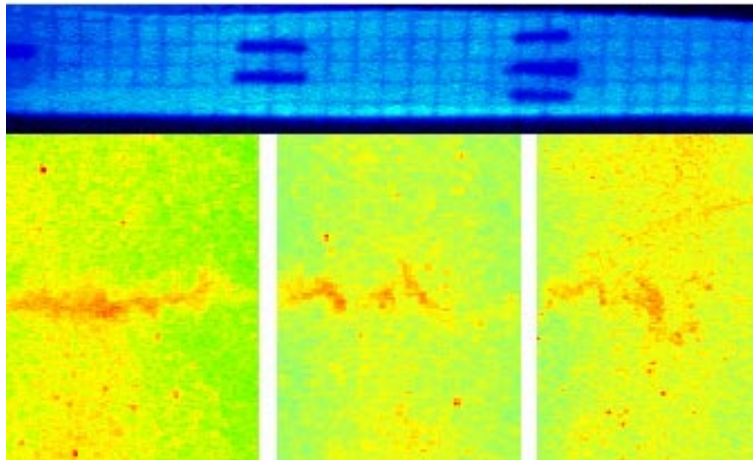


Figure 4 : Single pulse Rayleigh signal for $z = 10 - 38$ mm

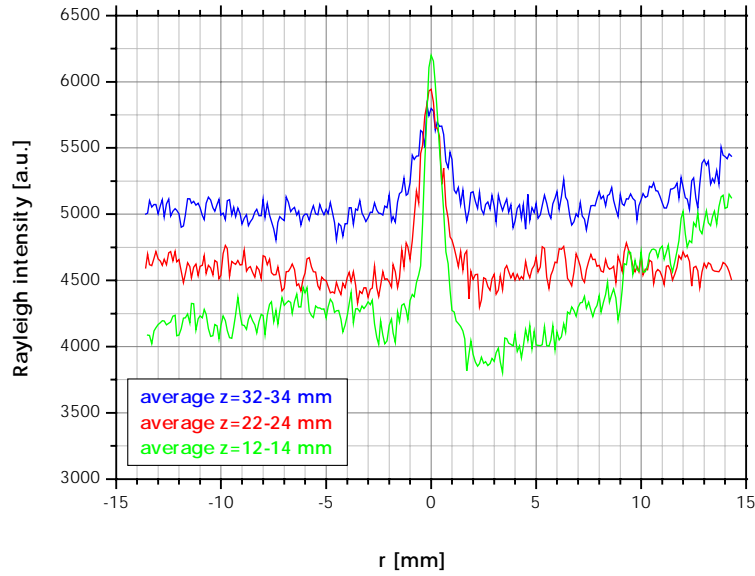


Figure 5 : Radial profiles of the Rayleigh scattering intensity averaged for $z=12-14\text{ mm}$, $z=22-24$, and $z=32-34\text{ mm}$.

2.3.2 Ignition Transient

According to the phenomenology observed the ignition transient can be divided into 4 phases. The ignition transient follows the general scenario:

- (i) As a result of the deposition of the laser energy a small flame kernel is formed, which is convected downstream. The OH-emission of this flame kernel is decreasing to a level, that is rather not detectable with the intensified high-speed camera. The size of this flame kernel is rather constant.
- (ii) After some time the movement of the flame kernel changes its direction and the flame kernel moves upstream. The size of the kernel is increasing and the OH-emission increases as well. Finally the flame is attached to the injector.
- (iii) The flame separates in a small region attached to the injector and a second region moving downstream. The downstream flame is consuming the unburned propellants and extinguishes after some time. The flame anchored at the injector is not visible in some tests but from the flame evolution it is obvious that it has to be existent. This flame is becoming longer and extending in the downstream direction.
- (iv) The flame stabilizes around the O_2 -jet, but extinguishes, when the combustion chamber pressure falls below a specific level.

Based on the experimental results the phenomenology of the ignition transient is discussed in detail in the following:

phase (i): Frames from the high-speed video of the OH-emission are shown in Figure 6. To see the whole story of flame evolution it is necessary to look even at the smallest intensities, in some cases the dynamic range of our camera is not high enough to detect the smallest OH-emission levels. For that reason in Figure 6 the raw-data and frames with enhanced gray-values (gray value interval [0-10] extended to [0-255]) are shown.

As a result of the deposition of the laser energy a small flame kernel is formed, which is convected downstream. The size of this flame kernel is rather constant. The OH-emission of this flame kernel is decreasing and rather not detectable with the intensified high-speed camera. Phase (i) ends about 0.3-0.4ms after ignition when the downstream convection of the kernel stops.

frame#	time [ms]	GGA05 raw data	GGA05 enhanced gray values
2	0.06		
4	0.17		
6	0.28		

Figure 6 : Flame kernel initiated by the laser induced spark and its downstream convection during phase (i)

phase (ii): After some time the movement of the flame kernel changes its direction and it moves upstream. The size of the kernel is increasing and the OH-emission increases as well. Finally the flame is attached to the injector. Frames of the OH-emission during this phase are shown in Figure 7. Simultaneously to the OH-intensity the combustor chamber pressure starts to increase as well (see Figure 8). The low pressure loss for H_2 at the injector results in a higher chamber pressure than in the H_2 -dome. Just after around 3ms the dome pressure is above the chamber pressure again.

OH-emission of the flame kernel is reaches a maximum near to 0.8ms. The upstream moving flame kernel has now attached to the injector.

The position of the upstream and downstream flame front as determined by image processing routines can be seen for test GGA04 in the left half of Figure 9 for 0-3ms after ignition. For $t \in [0.1\text{ms}, 0.4\text{ms}]$ the evaluated z_U and z_D are zero, because no flame has been detected by the image processing software. For $t > 0.7\text{ms}$ the flame is attached to the injector and $z_U = 0\text{mm}$.

In the right half of Figure 9 a zoom for $t \in [0.4\text{ms}, 0.7\text{ms}]$ - the time period when the flame kernel grows and moves upstream - is shown. The slopes of the linear fits to the flame front positions correspond to the front velocities v_U and v_D . As explained above with v_U and v_D the convection and flame-velocities can be evaluated. Based on the analysis of 6 tests with the 6mm-nozzle the mean convection velocity $v_c = -52 \pm 67\text{m/s}$ and the mean flame front velocity $v_f = 300 \pm 22\text{m/s}$ have been determined. The uncertainties given are the standard deviation due to the variation of results from tests to test. The negative convection velocity may be surprising, but can be understood by the pressure increase and related compression of the unburned propellants.

A peak chamber pressure of 6.8bar is reached after about 1.2ms (see Figure 8), the average slope of the pressure increase was 8.1bar/ms.

frame#	time [ms]	GGA05 raw data	GGA05 enhanced grey values
8	0.39		
10	0.50		
12	0.61		
14	0.72		

Figure 7 : Upstream movement and growing of the laser induced flame kernel during phase (ii)

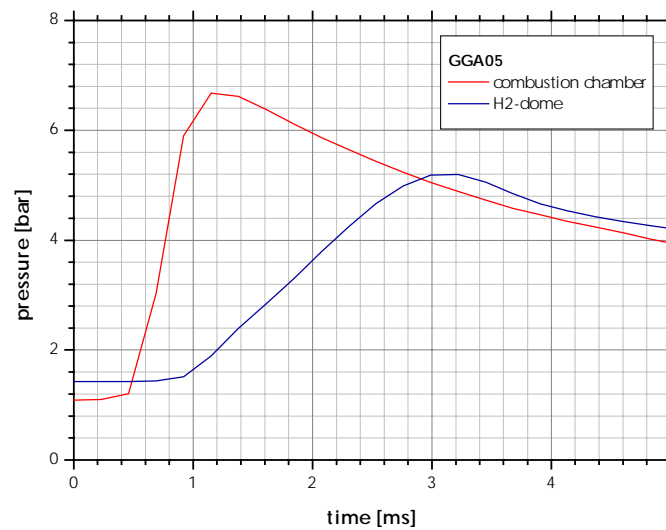


Figure 8 : Chamber pressure and H₂-dome pressure during the early ignition transient.

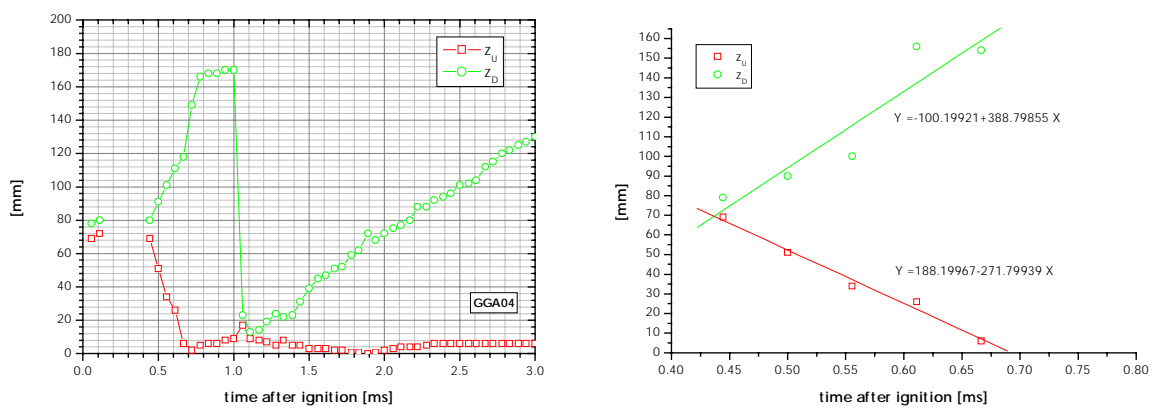


Figure 9: Positions of the upstream and downstream flame front (left) and linear fits to determine the flame front velocities during phase (ii) (right) for test GGA04, 6mm-nozzle

phase (iii): Between about 1ms and 3ms after ignition the flame separates in a small region attached to the injector and a second region moving downstream. Frames of the OH-emission during this phase are shown in Figure 10.

As soon as the upstream moving flame of phase (ii) has anchored at the injector the OH-emission is decreasing significantly (see frame #20, Figure 10). The anchored flame is even not visible in some tests but from the flame evolution it is obvious that it has to be existent during all the time. With increasing time the anchored flame grows along the downstream direction with associated increasing OH-emission intensity. The OH-intensity reaches a peak value around 3.5ms after ignition for the 6mm-nozzle. The length of the flame, i.e. the downstream flame front, as function of time is shown in Figure 11. The slope of this curve, i.e. the velocity with which the front moves downstream, has been determined for the time interval $t \in [1\text{ms}, 2.5\text{ms}]$. The mean value for the flame front velocity was $62 \pm 8\text{m/s}$ with the 6mm-nozzle. As can be seen in Figure 11 after 2.5ms the flame front velocity slows down.

The second downstream moving flame is shrinking, consuming the unburned propellants and extinguishes after about 2ms (Figure 10). From the positions of the upstream and downstream front of this flame the convection and flame velocities have been extracted. An example of the flame front positions during this phase for a test with the 4mm-nozzle is shown in left side of in Figure 11. For the tests with the 6mm-nozzles a convection velocity of $v_C = 12 \pm 22\text{m/s}$ and a flame velocity of $v_F = -101 \pm 32\text{m/s}$ are obtained. The negative flame velocity is (as it should be) consistent with the visible shrinking of the flame region.












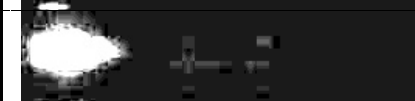
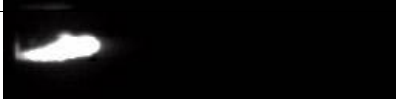
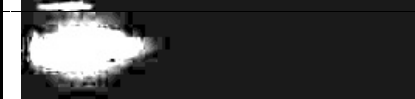
frame#	time [ms]	GGA05 raw data	GGA05 enhanced gray values
16	0.83		
20	1.05		
24	1.28		
28	1.50		
32	1.72		
36	1.94		
40	2.16		

Figure 10: Growing of the flame anchored at the injector and separation and burning out of downstream flame during phase (iii)

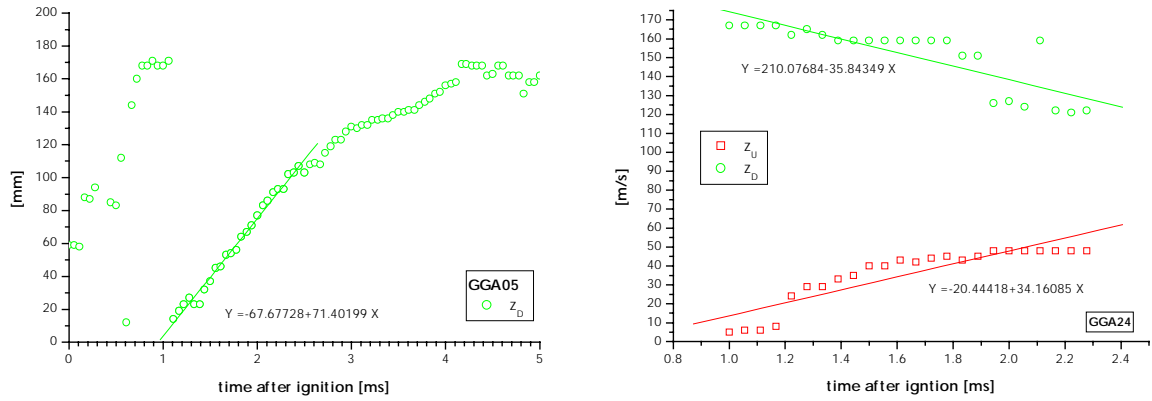


Figure 11: Left: downstream position z_D of the flame front attached to the injector (test GGA05, 6mm-nozzle); Right: movement of the fronts of the burning out downstream flame (test GGA24, 4mm-nozzle)

phase (iv): The flame stabilizes into a pencil like shape after about 5ms (Figure 12). As seen in Figure 13 the OH-emission intensity becomes now rather constant. The chamber pressure built up during phase (ii) has still not relaxed to stationary conditions at this time (Figure 8). During the pressure becomes smaller, the flame intensity decreases slowly, until the flame suddenly extinguishes. This happens at 17-19ms, when the chamber pressure falls below around 1.8bar.

With the 4mm-nozzle a stationary combustion chamber pressure of 2.6bar has been reached. No extinction of the flame during the time of observation (100ms) has been detected.

frame#	time [ms]	GGA05 raw data	GGA05 enhanced gray values
44	2.39		
50	2.72		
60	3.28		
70	3.83		
80	4.39		
90	4.94		
100	5.50		

Figure 12 : Sequence of OH-images during phase (iv)

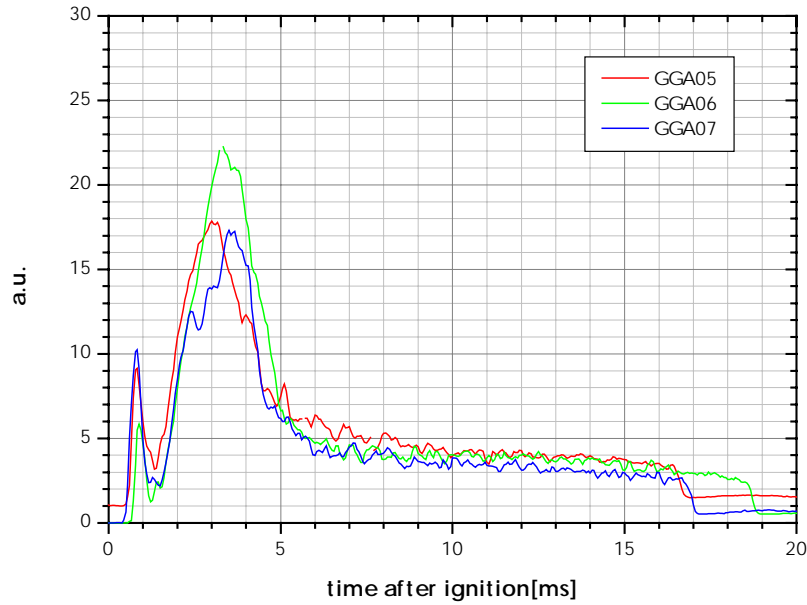


Figure 13 : Temporal evolution of the mean intensity of the OH-emission for three tests with the 6mm-nozzle.

2.3.3 Comparison of Tests with 6mm- and 4mm-Nozzle

The general ignition scenario is quite similar, independent whether the $\varnothing 6\text{mm}$ - or $\varnothing 4\text{mm}$ nozzle has been used. However, in some aspects there are differences. The characteristic data are listed in Table 2.

Until the laser induced flame kernel has attached to the injector (phases (i) and (ii)) with both nozzles similar characteristic times are observed, the convection velocities of the flame kernel are similar in the frame of the measurement accuracy for both configurations. The growth of the kernel however is significantly faster with the 6mm-nozzle than with the 4mm-nozzle.

The evolution of a conical flame anchored at the injector (phase (iii)) is clearly delayed for the $\varnothing 4\text{mm}$ -nozzle-tests. The velocity with which the leading flame front moves downstream is smaller by about 63% as compared to for the $\varnothing 6\text{mm}$ -nozzle tests.

A prominent difference is that the flame could be stabilized with the $\varnothing 4\text{mm}$ -nozzle at a stationary pressure of 2.6bar.

phase	event	6mm-nozzle	4mm-nozzle
(ii)	flame kernel: start of growing, upstream movement	0.4ms	0.4ms
	chamber pressure: start of pressure increase		
	flame kernel: convection velocity	$-52 \pm 67 \text{ m/s}$	$-37 \pm 52 \text{ m/s}$
	flame kernel: flame front velocity	$300 \pm 22 \text{ m/s}$	$171 \pm 59 \text{ m/s}$
	flame kernel attaches to the injector, peak OH-emission of flame kernel	0.8ms	0.8ms
(iii)	chamber pressure: slope	8.1bar/ms	11.9bar/ms
	chamber pressure: time of pressure peak	1.2ms	1.6ms
	chamber pressure: peak value	6.8bar	11.1bar
	anchored flame: time of downstream spreading	1-3ms	2-5ms
	anchored flame: downstream flame front velocity	$62 \pm 8 \text{ m/s}$	$39 \pm 5 \text{ m/s}$

	separated flame: convection velocity	12±22m/s	16±25m/s
	separated flame: flame front velocity	-101±32m/s	-29±8m/s
	separated flame: extinction	2ms	3.5ms
	anchored flame: time of OH-peak	3-3.5ms	6.5ms
(iv)	anchored flame: stabilization in pencil shaped form	5ms	8ms
	anchored flame: flame extinction	17ms	no extinction
	chamber pressure: stationary value	-	2.6bar

Table 2 : Characteristic data for tests with Ø4mm- and Ø6mm-nozzles.

2.4 Summary

There is indication from the Schlieren- and Rayleigh images that the regular Mach-pattern in the sonically injected oxygen leaves its mark on the length scale of jet-disintegration. Coherent structures originating in a H_2/O_2 -shear layer entraining H_2 into the O_2 -flow could not be seen, neither in the Schlieren, nor in the Rayleigh images.

During the first few milliseconds the combustion chamber pressure is above the H_2 -dome pressure. Thus the dynamics during phases (ii) and (iii) is influenced by the dynamic response of the H_2 -dome pressure on the transient combustion chamber pressure. During phase (iv) pressures in the H_2 -dome and combustion chamber are in dynamic equilibrium.

The reproducibility of the qualitative transient ignition phenomenology was good. Quantitative estimation of flame velocities were possible with variations in the order of 10%-30% from test to test.

A comparison of results with the 4mm and 6mm-nozzle shows, that although mixture ratio and injection conditions are similar at stationary cold flow, during the ignition transient flame-, convection-, and flame front-velocities are significantly different due to the different pressure conditions.

3 Modeling of H_2/O_2 Ignition Transient

The aim of the study is to select, among the numerous approaches used to study combustion phenomena [20], a combustion model, capable of predicting ignition transient of a liquid rocket engine using H_2/O_2 propellant systems, with a grid refinement allowing reasonable computational time. So, we have chosen a RANS approach with a kinetic model which can take into account a reaction mechanism characteristic of ignition process. Of course, because of the strongly non linear character of the source term, it could be erroneous to use the mean temperature to calculate source term except if the reaction rate is sufficiently slow compared to turbulence phenomenon. This is the case before ignition and we can consider that we are locally, i.e. in each cell in a perfectly stirred reactor. This kind of model has already been successfully used for the simulation of H_2/O_2 flame [23].

4 Numerical Simulation of Microcombustor Ignition Transient

Physical processes involved in this micro-combustor are of various types. We have to study here the ignition of a diffusion flame which is characterized by a reaction zone between oxidizer and fuel.

Moreover, the large volume of the chamber where oxygen and hydrogen are injected at high velocity enables large recirculation zones, promoting mixing of the propellants.

As mentioned earlier, the energy deposited into the chamber by the laser pulse produces locally a rapid pressure and temperature rise which generates a first pressure wave and modify locally the flow. Then the flame expands and this expansion modifies more globally the flow which interacts with the chamber dynamics.

Here, we intend to evaluate the new ONERA home-made code by comparing the previous experimental results with the simulation.

Due to the very small size of the laser spot and its off axis localization, the real phenomenon is 3D. But, due to the complexity of computation, numerical simulation will be preformed step by step. We have first developed a 2D axisymetric model to adjust cold flow simulation, laser phase simulation and spot localization and some other parametric studies.

Then a 3D model is built up and computations are performed to compare with experimental results.

4.1 The CEDRE code

4.1.1 Main features

CEDRE is the ONERA home-made code for numerical simulation of complex multi-physics flow in propulsion systems including :

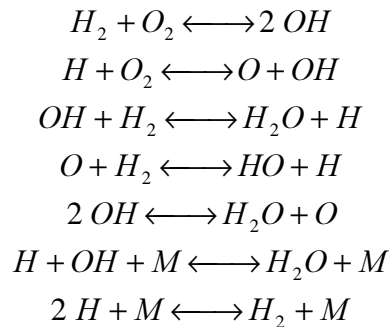
- reactive flow ;
- gaseous flow with particles (liquid and solid) ;
- heat exchange by conduction through the wall ;
- thermal radiation.

The CEDRE code is a multi-solvers and multi-domains code. To each phenomenon corresponds one solver. On the contrary of the former MSD code (see paragraph 5.2), CEDRE is written for non-structured grid. This means that each cell has an arbitrary number of faces and each face is composed of an arbitrary number of nodes. With this capability, It is possible to mesh complex geometry using any form of cell to mesh complex geometry. Connection between meshes and mesh refinement are easier to do. Hybrid meshes can also be used. The CEDRE code uses a gas solver named CHARME and two solvers for dispersed phase, an Eulerian solver name SPIREE and a Lagrangian one named SPARTE.

4.1.2 Combustion model

For hydrogen and oxygen, several kinetic schemes are available. However, the Eklund reduced kinetic scheme chosen for numerical simulation of coaxial supersonic jets has been successfully used and validated at ONERA in recent scramjet studies [21], where the predicted ignition length was in good agreement with experiment, and in rocket combustion modeling studies [23].

The Eklund mechanism involves 6 species in 7 reactions as follows :



4.1.3 Turbulence

The $k-l$ model is used to account for turbulence effects with the usual constant values, which is well adapted for internal flows.

4.2 Mesh

4.2.1 Mean features

Injection mass flows have been chosen according to table 1. A nozzle diameter of 4mm has been assumed in order to avoid supersonic flow in the oxygen pipe. The actual injector and chamber geometries were used except for the chamber exit where a straight tube was replaced by a classical convergent-divergent nozzle in order to set the location of the sonic line and to avoid numerical difficulties.

4.2.2 2D axi-symmetrical mesh

In order to validate this slightly modified geometry, we first compute a 2D axi-symmetrical representation of the chamber. We define an equivalent radius by keeping the same cross section as in the actual chamber; this gives :

$$\pi R^2 = L^2 \Rightarrow R = \frac{L}{\sqrt{\pi}} = \frac{60}{\sqrt{\pi}} = 33.85 \text{ mm}.$$

Figure 14 presents the geometry used for the 2D axi-symmetrical computation.

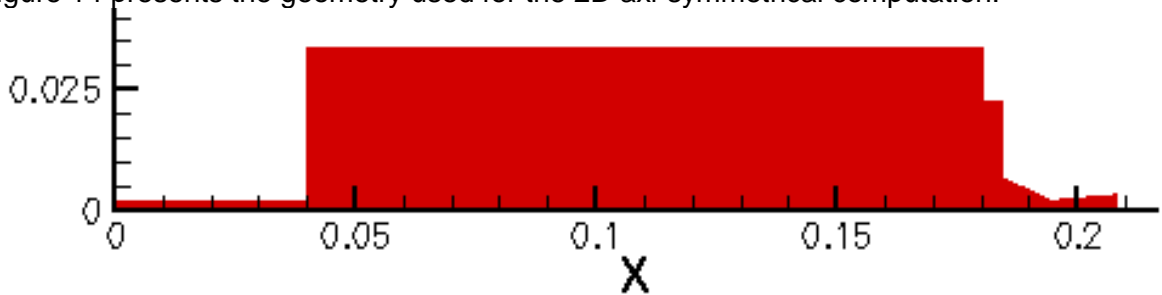


Figure 14 : 2D axi-symmetrical geometry

There is only one computational domain with 17650 elements and 1002 boundary faces.

4.2.3 3D mesh

Due to the punctual deposit of the laser energy, the flow is not symmetric around the chamber axis (X) and a 3D computation is required to represent as correctly as possible the experiment. As the laser spot is situated in the symmetry plane, only the half the chamber was meshed. The 3D grid contains 500 194 cells and 47 234 boundary faces (Figure 15).

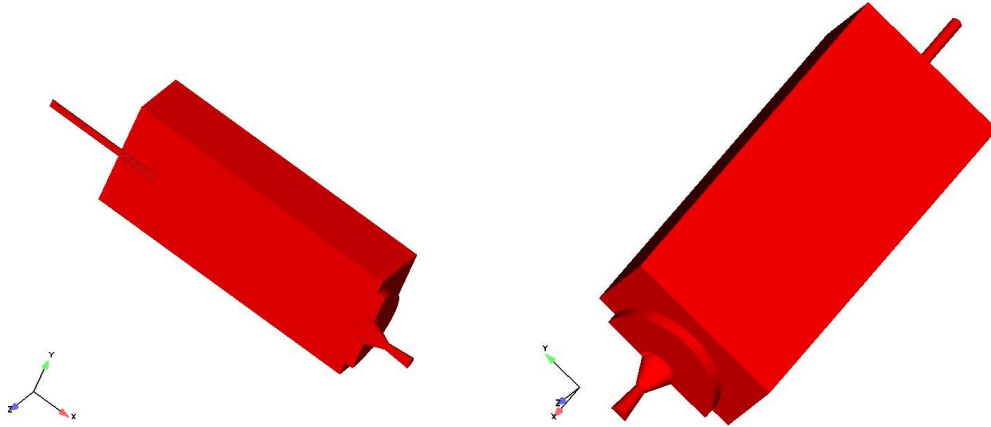


Figure 15 : Computational 3D geometry

4.3 Computation conditions

4.3.1 Boundary conditions

For boundary conditions, we have a constant injection mass flow at the inlet :

	O2	H2
Mass flow (g/s)	1.15	0.575
ρU (Kg/s/m ²)	983.76	61.01

As the k - l turbulence model is used, boundary conditions for k and l are also needed. The turbulence scale l was chosen equal to 10% of the hydraulic diameter. This leads to l equal to 10^{-4} m for both hydrogen and oxygen flows. The turbulence rate : $\tau = \frac{\sqrt{2k}}{U}$ gives the boundary value of k . τ is approximately equal to 1%. This leads to the following values for k .

- Oxygen flow: $U \approx 200$ m/s and $k = 2$
- Hydrogen flow: $U \approx 280$ m/s and $k = 4$

For the outlet condition, a constant pressure equal to 0.8 bar is imposed until the flow becomes supersonic at the nozzle exit.

In $Z=0$, there is a symmetry condition. An adiabatic condition is prescribed at the wall.

4.3.2 Initial conditions

As initial conditions for the steady-state cold flow, the whole computational domain is filled with hydrogen at a pressure is of 2.5 bar and a temperature of 285°K.

The stationary cold flow is used as initial conditions for transient computation.

4.4 Computations

4.4.1 2D axi-symmetric computation

4.4.1.1 Steady-state in cold flow conditions

The available data from “cold flow” experiment are injected mass flow rates, chamber pressure and O_2 density profile from Rayleigh signal measurements (Figure 5). In order to compare experiment and simulation, we plot O_2 repartition in the chamber . Three values of the turbulent Prandtl and Schmidt number were tested. 0.9 is the default value proposed by CEDRE; 0.7 is a more common value used for simulation of jet in a quiet atmosphere [22]. And 0.5 is used to see the influence of high diffusivity of hydrogen. Figure 16 shows oxygen mass fraction contours for the Schmidt number (Sc) equal to 0.7 in the upper half chamber and 0.9 in the lower half chamber. One can see that, for $Sc=0.7$, oxygen is trapped in the large recirculation zone .

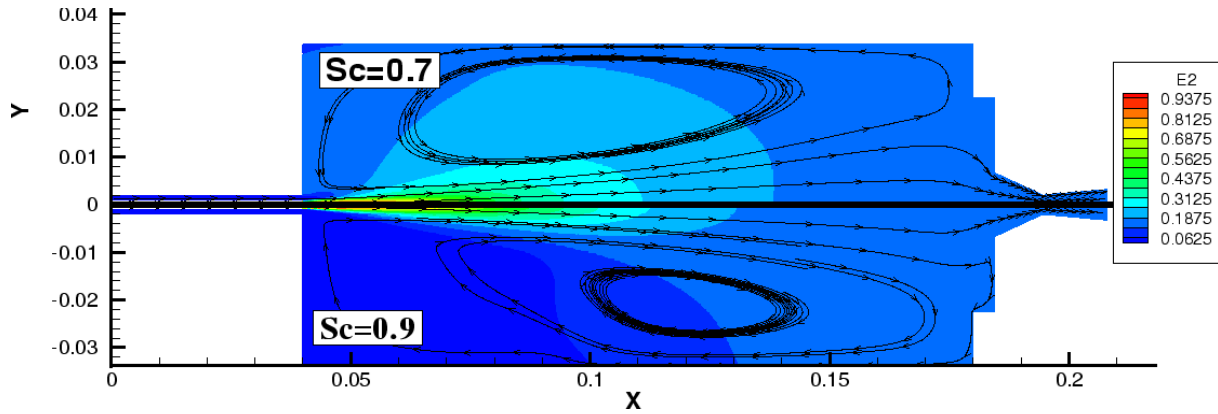


Figure 16 : Oxygen repartition in the 2D axi-symmetrical chamber

In order to compare more precisely with experimental data, radial profiles of the oxygen mass fraction in planes situated at 13 and 33 mm downstream the faceplate are presented in Figure 17 :

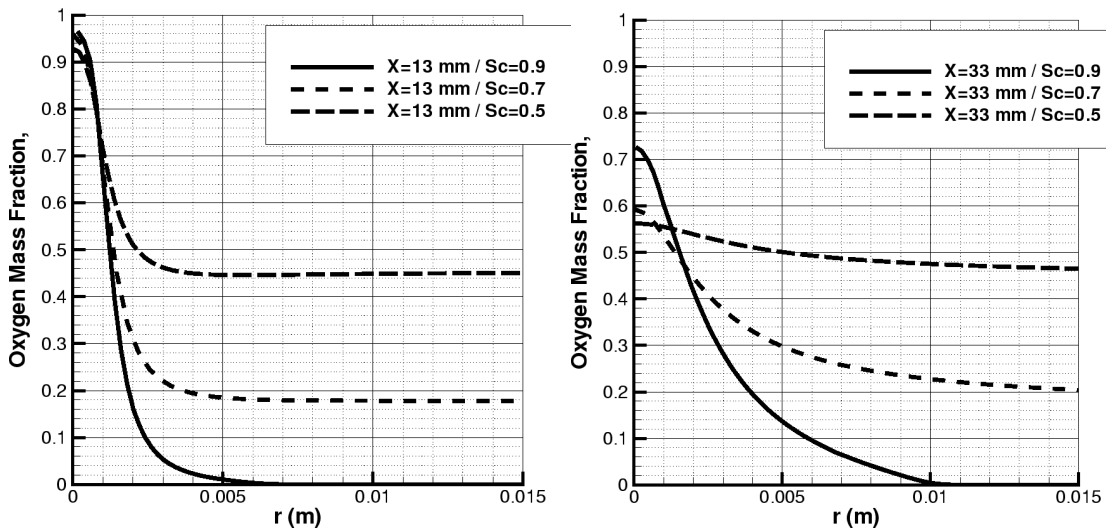


Figure 17 : Radial profiles of oxygen

Results show a great influence of turbulent parameters on the oxygen mass fraction in the recirculation zone. Near the injector ($x=13$ mm), this influence is nevertheless small close to the chamber axis. At location $x=33$ mm, the Schmidt number influences oxygen mass fraction on the axis but it is difficult to compare with experimental data because, at this location, the peak is quite merged with noise signal (Figure 5). Nevertheless, it seems that simulation agrees well with experiment in term of amplitude ratio with $Sc=0.7$, even if the second peak is smaller than experimental one.

The pressure inside the chamber is around 2,2 bar. It is in agreement with the experimental data.

4.4.1.2 Preliminary results under ignition conditions

Actual physical phenomena involved in the laser ignition (see paragraph 2.1.2) can not be reproduced with the current model. So, laser pulse is represented by a source term in the energy equation for cells corresponding to the laser location described in paragraph 2.1.2. Nevertheless, several locations were tested during these preliminary tests. Then source term is switched off when temperature reaches 4000 K which is the upper limit of thermodynamical coefficients representation in CEDRE.

The following numerical results correspond to $Sc=0.7$. To increase the ignition probability, the pulse laser is located in zone where the mixture ratio is stoichiometric which differs to the experiment location. This location gives, today, the larger flame kernel. Figure 18 presents temperature, OH mass fraction and O_2 mass fraction at the same instant as in the experiments.

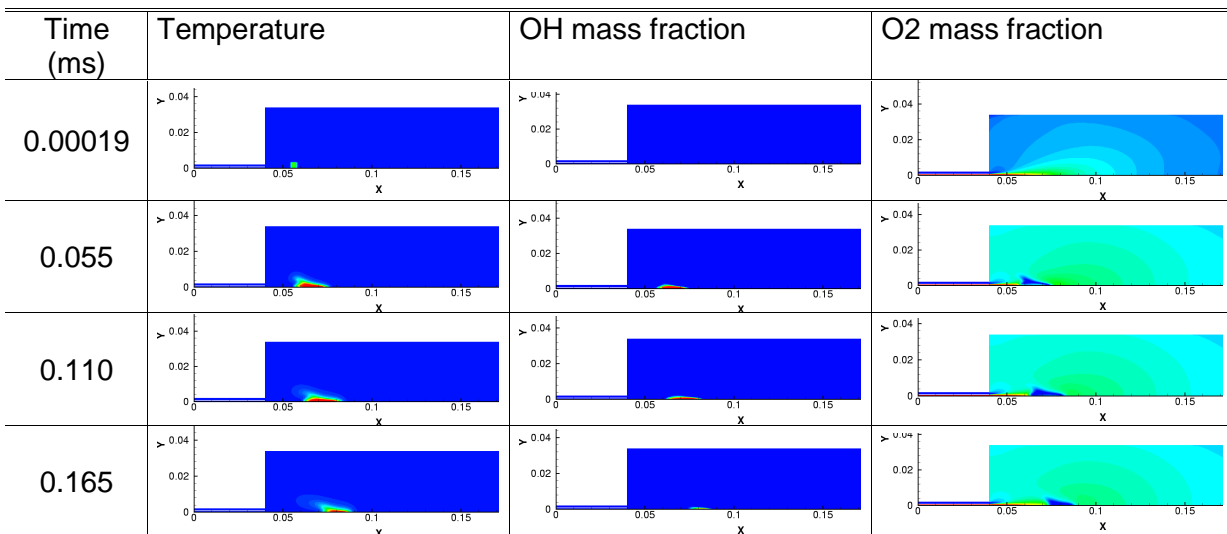


Figure 18 : Temperature, OH- mass fraction, and O_2 -mass fraction during ignition transient

The various tests performed with this model show that high temperature spot initiates OH formation which propagates in regions where mixture ratio is equal to 8. Then there is a propagation upstream and downstream but the propagation velocity is not sufficient to allow the flame to anchor at the injector. Then the flame kernel is carried away in the oxygen core where the flame extinguishes by lack of hydrogen.

It is important to notice that the laser pulse induces a high temperature and also a pressure peak which propagates and modifies strongly the flow field and the mixing outside of the jet as it is shown in the following pictures :

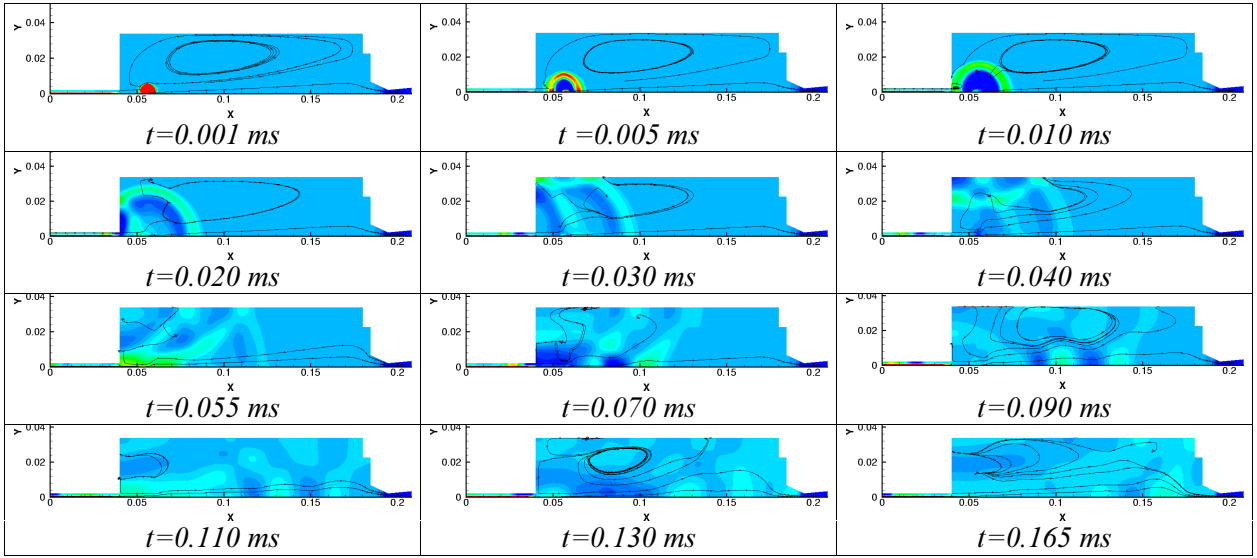


Figure 19 : Propagation of initial pressure peak

These 2 D computations induce the following remarks :

- modelization of laser pulse can be performed by a source term in energy equation.
- chemical reaction are initiated due to high temperature and pressure spots and develops
- initial pressure peak modify strongly the flow and it was important to describe as well as possible these expansion ;
- axisymmetrical configuration induces an axisymmetrical ignition which does not allow a strong interaction of the pressure waves with the jet which may increase mixing and promote propagation of the flame.

4.4.2 3D computation

For the 3D analysis, the first step was to get the steady-state cold flow before ignition. Figure 15 shows the computational domain. Due to large computational time, induced by the large volume of the chamber and small velocities, this computations have not yet completely converged.

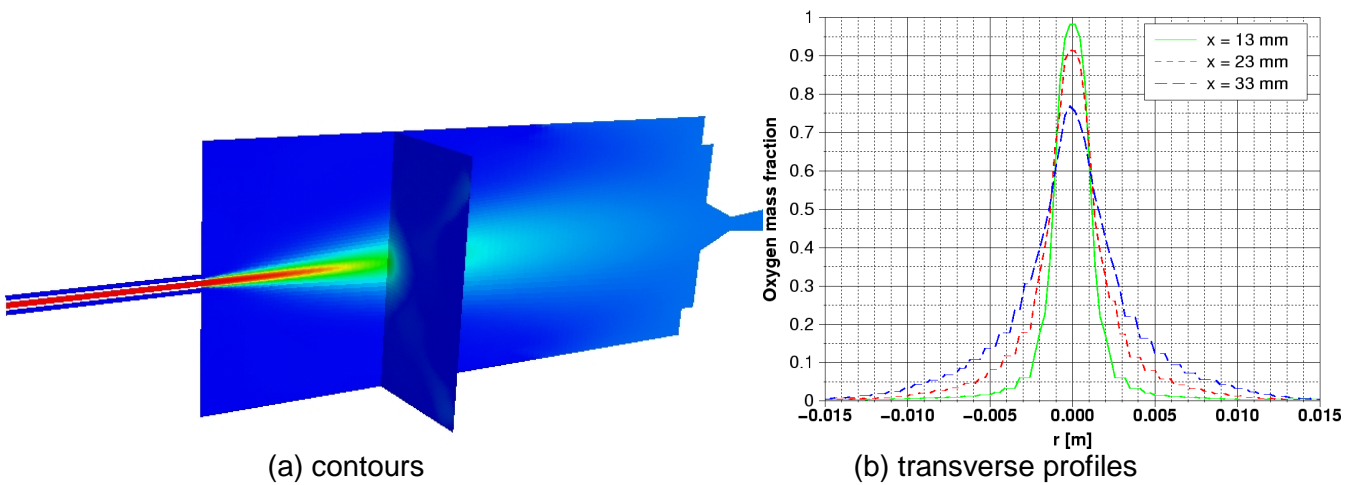


Figure 20 : Oxygen mass fraction

Figure 20 and 21 show examples of results. Figure 20-a shows oxygen mass fraction contours in the mid plane and in a transverse plane. The profiles of figure 20-b are coherent with those obtained in 2D axisymmetrical computations for $Sc=0.9$ (Figure 16 and 17).

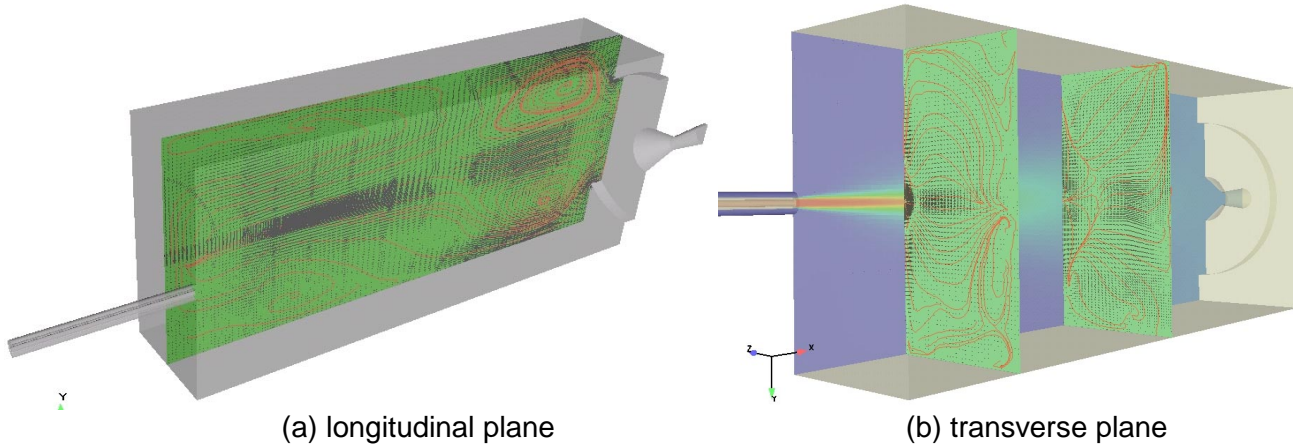


Figure 21 : Velocity vector and streamlines

Figure 21, (a) and (b), shows velocity fields and streamlines in a longitudinal plane and in two transverse planes, respectively. It is very interesting to notice the very complex nature of the flow. As in the 2D case, Figure 21 shows large vortices which fill nearly the entire chamber with two small vortices near the nozzle.

After the steady-state is reached, ignition calculation will be carried out.

5 Application to VINCI engine ignition

5.1 Introduction

This part describes calculations performed as a support of the VINCI engine development, using a simplified configuration. Effectively, the igniter configuration, chosen for the VINCI, is a torch jet parallel to coaxial injector flows, in order to meet the multiple ignition requirements, without damage for igniter hardware.

The torch jet is composed of burnt products issued from combustion of hydrogen with oxygen, i.e. water, intermediate species as OH radical and propellant in excess. Due to high pressure in the igniter chamber compared to main chamber pressure before ignition, the flow field exhibits the complex structure of under-expanded jets with shocks and expansions, modifying the composition of hot gas exiting the torch.

The classical design criterion is based on the amount of energy transferred from the igniter jet to fresh propellant flowing through the first row of coaxial injectors surrounding the igniter exit. Indeed, atomization and turbulence enable mixing of hydrogen and oxygen to produce an ignitable mixture, which is easy because the regions of inflammability are very extended in term of hydrogen diluted with oxygen. Then, heat is brought to this mixture by diffusion and mixing of the fresh mixture with the burnt products of the torch jet (turbulent diffusion). Moreover, when the hot gas jet is produced with the same propellants than those injected in the combustion chamber, as it is the case in the VINCI engine, chemical reactions could play an important role with respect to thermal effect in the chamber ignition.

Even if, a priori, mixing will involve the hot gas jet with fresh propellant flowing through the first injector row, the flow around the studied zone could be influenced by the pressure evolution and gradients in the whole chamber. That is why we have considered the actual geometry of the VINCI, nozzle included, to define the computational domain.

Up to now, computations applied to actual engines have been performed assuming that combustion time was negligible compared to turbulent time (high or medium Damkohler number). Combustion models assume a one-step complete combustion reaction, without dissociation, overestimating combustion and temperature, but they are not able to predict neither local extinction nor self ignition, since finite kinetic effects are not included in this kind of models. In fact, ignition modelization requires kinetics modeling. Like in the simulation of microcombustor experiment, the Eklund scheme was selected.

5.2 MSD Tool

These computations have been performed with the ONERA first generation code, named MSD. It is a three-dimensional code allowing simulation of two phase, multi-species, reactive flows. Contrarily to the CEDRE code presented previously, it uses structured grids. In the present study, only gaseous species are considered and the unsteady Reynolds-Averaged Navier-Stokes equations are solved along with species and turbulent quantity conservation equations. The space discretization is based on finite volume techniques on curvilinear structured grids, the convective fluxes being calculated on the cell interface using a flux-difference-splitting derived from the Roe scheme. The time integration implicit with second-order accuracy. The implicit algorithm uses a classical ADI factorization.

5.3 Geometry and Grid

One main phenomenon that needs to be well represented here is the interaction of the hot gas jet from the igniter with the first row of injectors. In order to reduce the complexity of the computation, we have chosen a 2D axisymmetrical configuration. The ratio between chamber radius R_{ch} and injector width δr is close to 1000. Moreover, the chamber is long enough to satisfy the requirement of heat transfer to hydrogen flow needed to drive the turbines and close the expander cycle, leading to a large volume. As a consequence, regular mesh of the chamber would have necessitated some millions of cells.

Computational performance of MSD in the case of kinetics is about $2\mu s$ /iteration/cell/equation. Estimation of computational time on a regular mesh of the whole chamber leads to a value as large as $4 \cdot 10^8$ s (i.e. 122 000 hours) for 0.1 s of real time.

It appears that the time of simulation becomes prohibitive and that one needs to relax some criteria. As one of the process to be well represented is the interaction of the jet and the first injector row, the grid was refined around this first row. So a drastic reduction of cell number was applied using mesh with variable grid size. In the same way, as the model is axisymmetrical, the assumption was made that modeling of the symmetrical injector was not necessary. Then we simulate the first row of coaxial injector by two rings whose areas are computed in order to have the same injected mass flow rate and injection velocity as in VINCI engine. In order to keep, as well as possible, the total injected momentum at injection plate, we have represented the second row by an annular zone containing only one cell with a simultaneous injection of the two propellants. The other injector rows have been modeled using uniform and simultaneous injection of the two propellants. The resulting mesh contains two domains (see Figures 22 and 23); the first one with 13×11 cells, and the second one with 73×54 cells.

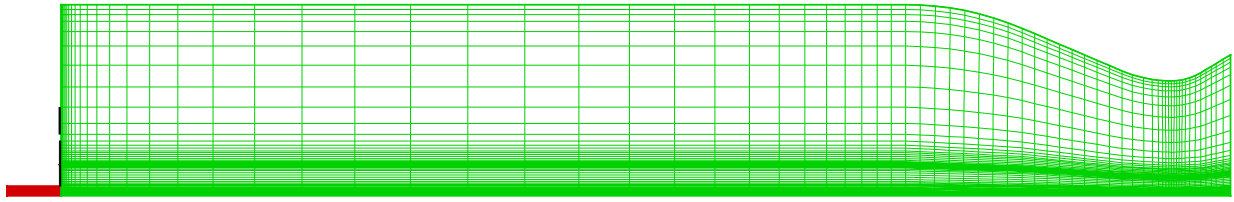


Figure 22 : Mesh

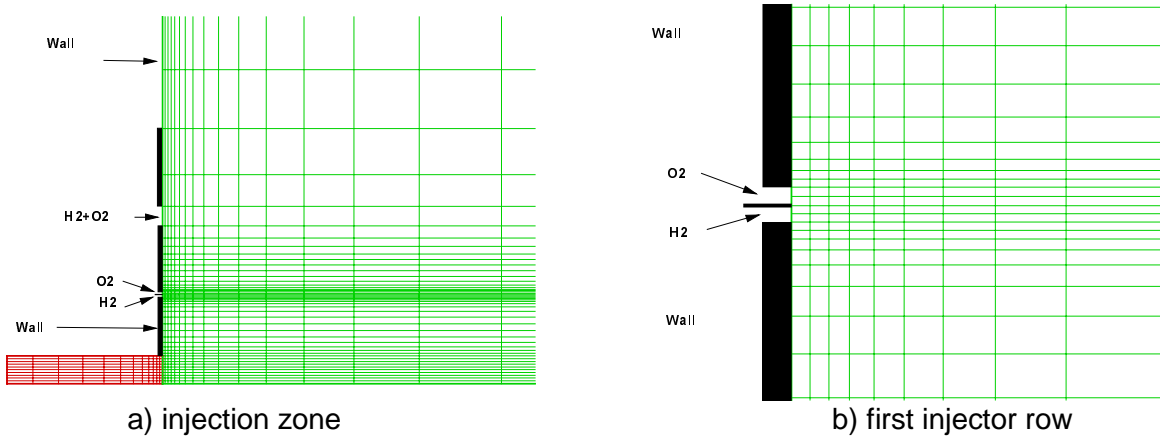


Figure 23: details of the grid

5.4 Computations

Several computations were performed to study the influence of parameters such as mixture ratio, sequence, initial pressure on ignition transient. The most important parameter, for the computational time is the ignition sequence. Considering that oxygen must be injected the last in order to avoid undesirable oxidation, two ignition sequences have been considered. The first one (sequence A) corresponds to the ignition of the igniter followed by injection of hydrogen, then injection of oxygen. The second sequence (sequence B) is the injection of hydrogen prior to ignition of the igniter. In any case, evolution of the injected flow of propellants are assumed to be a succession of ramps. Two values were assigned to the slopes of the ramps. At the end, eight combinations could be considered.

5.4.1 Boundary conditions

Boundary conditions are of four types :

- Viscous wall with wall functions
- Constant pressure at the nozzle equal to initial pressure until the flow becomes supersonic at the nozzle exit. Then the boundary condition is switched to a supersonic exit.
- For the igniter, the mass flow is assumed constant and the composition of hot gas is that of H_2/O_2 combustion products in equilibrium at a given mixture ratio. When there is no flow, mass flow condition is replaced by wall condition.
- For hydrogen and oxygen injection, the temporal evolution of the mass flow rate was prescribed and depends on the ignition sequence. Cold gaseous hydrogen is injected. Oxygen is also injected gaseous at saturation temperature. When there is no flow, mass flow condition is replaced by wall condition.

5.4.2 Initial conditions

Two initial conditions were assumed corresponding respectively to sea level ignition and in-space ignition. For the first one, the chamber is filled with air at 1 bar and room temperature. For the second one, the chamber is filled with cold pure hydrogen at 60 mbar.

5.5 Results

Among the eight parameter combinations presented in paragraph 5.4 only two of them are presented hereafter :

- Sequence B, sea-level conditions, short chronology ;
- Sequence B, in-space conditions, short chronology.

Many data are obtained from these unsteady computations as pressure and mass flow rate evolutions. Main thermodynamics variable fields are also stored.

Hereafter, only pressure evolutions are reported for first injector exit plane (H_2 and O_2) and at wall between the first two injectors. OH and water fields are shown just before the pressure peak and just after (figures 24 and 25).

Sequence B, sea-level conditions;

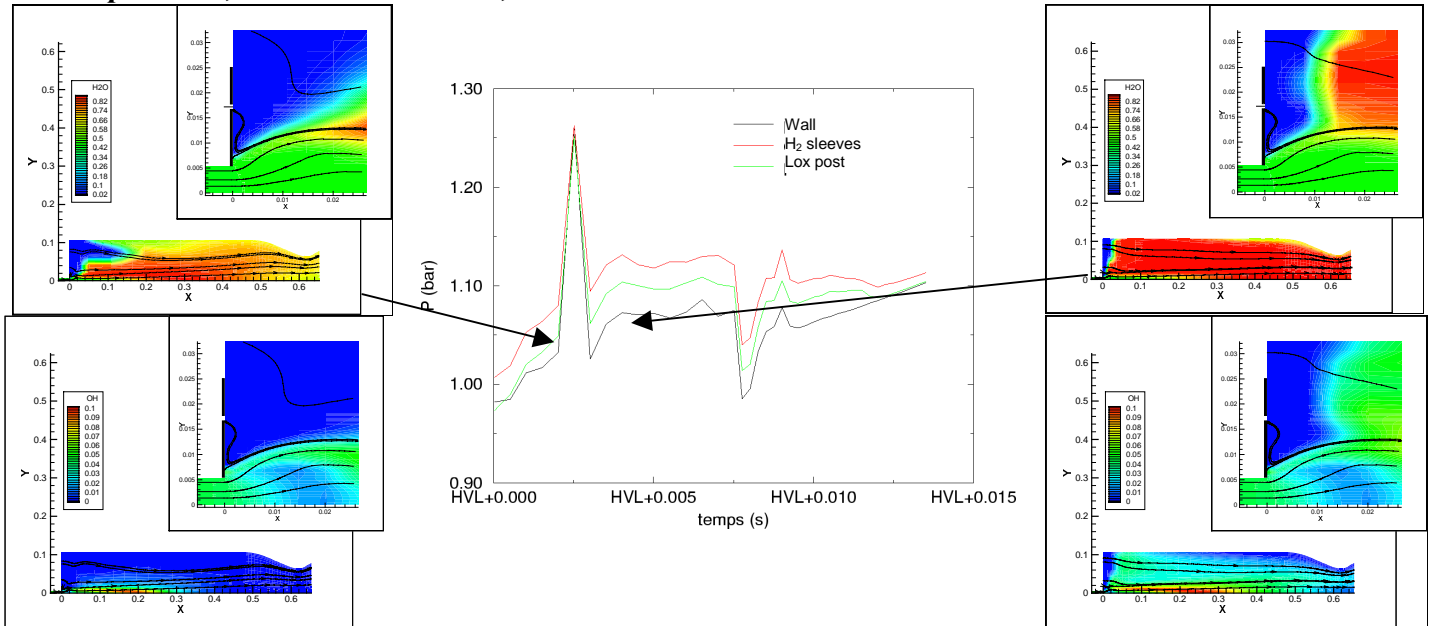


Figure 24 : Pressure at faceplate and contours of H2O and OH

The igniter hot gases contain OH element. Nevertheless, looking at OH mass fraction contours, the maximum value is encountered along the jet boundary. This seems to indicate the initiation of combustion, the jet being oxygen rich. Simultaneously, the evolution of water mass fraction contours seems to indicate that combustion goes first downstream and then propagates upstream towards the injection plate.

Sequence B, vacuum conditions ;

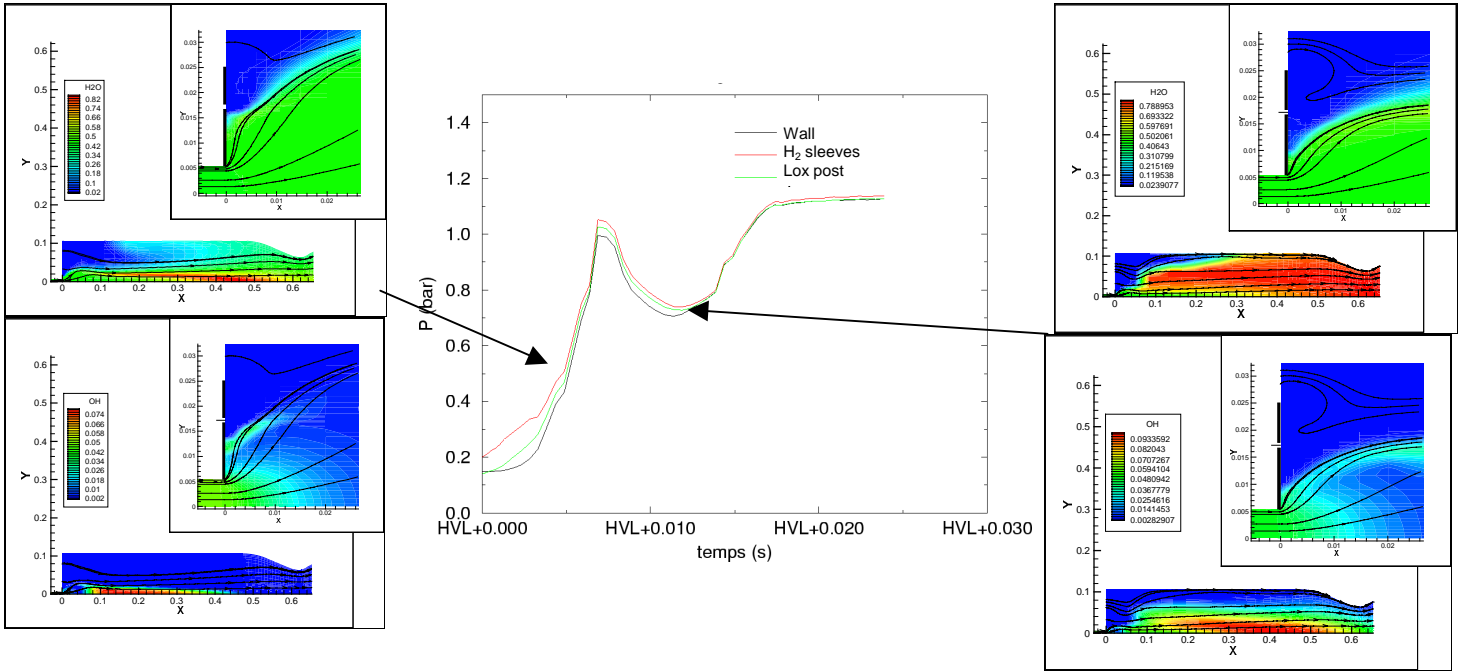


Figure 25 : Pressure at face plate and contours of H₂O and OH

Figure 25 shows similar results under partial vacuum conditions. As in the preceding case, ignition of chamber mixture occurs at the end of the torch jet. Due to low pressure conditions, the hot gas jet is more expanded and the OH maximum mass fraction is located more downstream than in sea level conditions. Looking at water mass fraction contours, one can see that combustion propagates upstream less quickly than in sea level conditions.

Figure 26 presents OH and H₂O contours during the entire transient period for both conditions.

Analysis of the whole set of results seems to indicate that chamber ignition takes place in a zone where the temperature is high, the mixture ratio is close to 8 and the Mach number close to the unit. That corresponds to the first third of the chamber for a ignition at the atmospheric pressure and the second third in the case of the partial vacuum. The analysis of the curves for partial vacuum ignition (60 mbar) shows in addition that the relaxation of the jet generates close to the injector a temperature fall in limit of jet being accompanied by a slip line, preventing the mixture of hot gases with fresh propellants.

Lastly, from a system point of view, it is useful to observe the evolution of the ignition delay in various simulations. The ignition delay is defined as the time between the Lox valve opening, and the first maximum of pressure. It thus appears that the oxidizer-rich torch jet reduced the ignition delay, but that partial vacuum led to an increase of this delay.

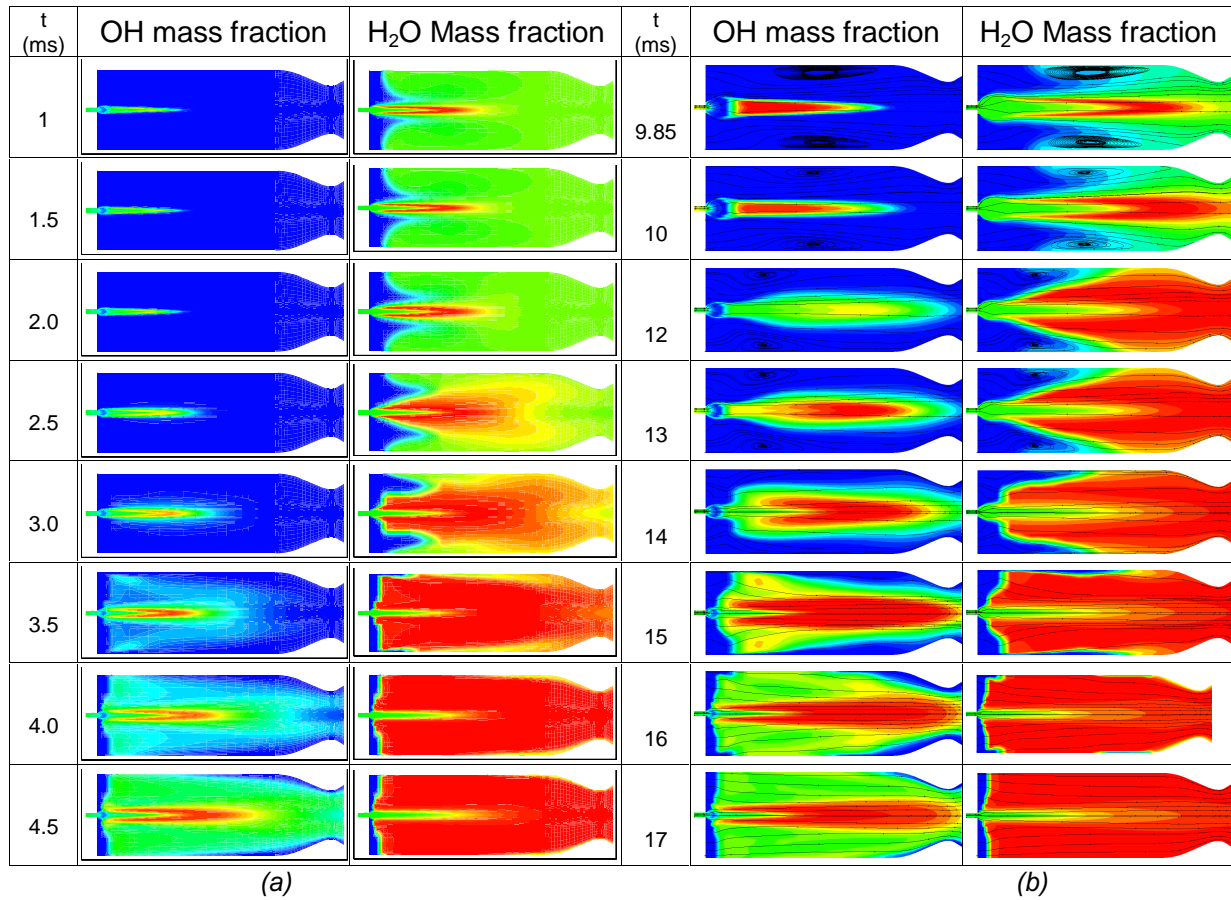


Figure 26 : Contours of OH and H₂O mass fraction : (a) sea level, (b) vacuum

5.6 Summary

This study showed that the use of chemical kinetics led to an ignition of the combustion chamber, without using an arbitrary criterion as in the models with infinitely fast chemistry. The follow-up of the intermediate species, in particular OH radical, made it possible to locate the initiation then the propagation of combustion. Two conditions of external pressure (1 bar and 60 mbar) showed that the point of ignition was located at the end of the igniter flame, where one finds simultaneously a mixture ratio close to stoichiometry, Mach numbers lower than unity and high temperature. In all the cases, ignition results in a peak on the temporal evolution of pressure and the outgoing flow which makes it possible to define an ignition delay starting from the opening of the oxygen valve.

From a simulation point of view, we can expect the peak of pressure is not representative of reality because, on one hand, the implicit scheme is applied to combustion source terms. In addition, energy release is realized on the volume of the cell, which is relatively large at the ignition location. On the other hand, the flame growth takes place in a homogeneous medium, due to the hypothesis of uniform premixed injection for the external rows, which is not the case in reality where flame propagation from one injector to another could be completely different.

Thus, new calculations with more representative geometry of the injection elements is under way. It should be then possible to study the influence of the starting sequence and the external pressure on the ignition time.

6 Conclusions

Numerical simulation is more and more needed to predict system behavior during start up and main stage operations to reduce cost development and limit full scale tests. Current activities on ignition of liquid rocket engine include fundamental studies (experiment and simulation) to develop more representative models as well as the use of existing tools to help designing ignition systems and predicting the engine behavior during start up.

Basic experiments as those developed at DLR are necessary to understand elementary processes involved in rocket engine ignition transient and show how the flow dynamic interact with combustion processes. The diagnostics allow to build up a database useful for code validation.

Preliminary 2D calculations allow to adjust the numerical ignition procedure which initiates combustion in a flame kernel which develops in the flow. Although these 2D calculations are necessary as a first step to address this complex problem, they can not allow to reproduce actual ignition transient observed in the experiment. They have raised some questions about refinement of the grid, location of the laser pulse and turbulent coefficient which have been accounted for in the 3D computations. Calibration of the model using the microcombustor data should improve the reliability in the numerical simulation in predicting rocket engine ignition transient.

Acknowledgement

The support of CNES is gratefully acknowledge for the Vinci studies.

References

- [1] E. Hurlbert, R.J. Moreland, Propellant Ignition and Flame Propagation, Proceedings of the 2nd International Symposium on Liquid Rocket Propulsion, Chatillon, 1995
- [2] P. Alliot, V. Jover, J.N. Caruana, J.P. Dutheil, A. Juhls, Ariane 5 Cryogenic Upper Stage Propulsion Systems, AIAA 2001-3259
- [3] G. Frenken, E. Vermeulen, F. Bouquet, B. Sanders, Development of the Ignition System for Vinci, 4th International Conference on Launcher Technology "Space Launcher Propulsion", December 3-6, 2002, Liege, Belgium
- [4] G. Ordonneau, H. Douchet, Numerical Simulation of the Vinci Thrust Chamber Ignition, 4th International Conference on Launcher Technology "Space Launcher Propulsion", December 3-6, 2002, Liege, Belgium
- [5] C. Hensel, D. Wiemann, W. Oechslein, J. Görden, Ignition Aspects for the Vinci Thrust Chamber, AIAA 2002-4008
- [6] J. Gastal, Ariane 3rd Stage Ignition Improvement, AIAA 88-2931
- [7] D. Preclik, P. Spagna, Low Frequency and High Frequency Combustion Oscillation Phenomena inside a Rocket Combustion Chamber Fed by Liquid or Gaseous Propellants, AGARD CP-450
- [8] K. McManus, F. Aguerre, B. Yip, S. Candel, Analysis of the Ignition Sequence of a

Multiple Injector Combustor Using PLIF Imaging, Non Intrusive Combustion Diagnostics, K, Kuo, T. Parr (Eds.), Begell House, 1994

- [9] V. Quintilla, M. Cazalens, R. Lecourt, G. Lavergne, Experimental and Numerical Study to Predict Spray Ignition, Proc. Of ILASS-Europe 2001, (Zurich), (2001).
- [10] R.A. Bjorklund, Very Low Thrust Gaseous Oxygen-Hydrogen Rocket Engine Ignition Technology, 20th JANNAF Combustion meeting, Vol. 1, D.S. Eggleston (Ed.), CPIA PUBL-383, Laurel, MD, 1983, pp. 699-711.
- [11] D.R. Ballal, A.H. Lefebvre, Ignition of Liquid Fuel Sprays at Subatmospheric Pressures, Combustion and Flame, Vol. 31, pp. 115-126, 1978.
- [12] M. Arai, H. Yoshida, H. Hiroyasu, Ignition Process of Compound Spray Combustible Mixtures, Dynamics of heterogeneous Combustion and Reacting Systems, Progress in Astronautics and Aeronautics, Vol. 152, 1993.
- [13] O. Gurliat, V. Schmidt, O.J. Haidn, M. Haidn, Ignition of Cryogenic H₂/LOX-Sprays, submitted for publication to Aerospace Science and Technology, 2003
- [14] P.A. Baudart, V. Duthoit, J.C. Harlay, Numerical Simulation of Cryotechnic Rocket Engine Ignition, AIAA 91-2290, 1991
- [15] P.A. Baudart, V. Duthaut, T. Delaporte, E. Znaty, Numerical modeling of HM7 B main chamber ignition, AIAA 89-2397, 1989
- [16] P.D. Maker, R.W. Terhune, C.M. Savage, Optical Third Harmonic Generation. In III International Conference on Quantum Electronics Proceedings, Paris, 1963
- [17] Y.-L. Chen, J.W.L. Lewis, C. Parriger, Spatial and Temporal Profiles of Pulsed Laser Induced Plasma Emissions, Journal of Quantitative Spectroscopy and Radiative Transfer, 67, 2000, pp. 91-103
- [18] J.A. Syage, E.W. Fournier, R. Rianda, R.B. Cohen, R.B., Dynamics of Flame Propagation using Laser-Induced Spark Ignition: Ignition Energy Measurements, J. Applied Physics 64-3, 1988, pp. 1499-1507.
- [19] I.P. Shkarofski, Review of Gas-Breakdown Phenomena Induced by High-Power Lasers I, RCA Review, Vol. 35, 1974, pp. 48-78
- [20] S. Candel, D. Thévenin, N. Darahiba, D. Veynante, Progress in Numerical Combustion, Combustion Science and Technology (1999) Vol 149, pp297-337
- [21] D. Gaffie, U. Weppeler, Ph. Magre, W. Koschel, Ph. Novelli, Numerical Investigation of Supersonic Reacting Hydrogen Jets in a Hot Air Coflow, AIAA 2001-1864, Kyoto, Japan, April 2001
- [22] J.O. Hinze, Turbulence, Mac Graw-Hill, Inc, Second Edition (1987)
- [23] Proceedings of "Workshop on Rocket Combustion Modeling : Atomization, Combustion and Heat Transfer", ONERA, March 11-13, 1998, Toulouse, France